Hindawi
International Journal of Optics
Volume 2019, Article ID 3573976, 10 pages
https://doi.org/10.1155/2019/3573976

Research Article

Properties of Gaussian Beam Propagating in Ring Resonator Sensor

Long Jin, Zhiqiang Yang, and Qiang Zhang

Department of Basic Science, Hubei University of Automotive Technology, 167 Checheng West Road, Shiyan City 442002, Hubei province, China

Correspondence should be addressed to Long Jin; crazyjinlong@163.com

Received 18 November 2018; Accepted 3 February 2019; Published 3 March 2019

Academic Editor: Giancarlo C. Righini

In this paper, we deduce the paraxial analytical expression for the Gaussian beam propagating in the sandwich slab system which contained double negative material based on light transfer matrix and generalized Huygens-Fresnel integral equation; the evolution properties of emerging Gaussian beam contour graph intensity distribution on the receiver plane, the relation between beam spot size and negative refractive index coefficient, and beam side transmission view in slab system changed with three negative refractive index parameters are illustrated through numerical examples. What is more, we propose a ring resonator sensor to measure the concentration of NaCl solution on the basis of above theory, of which the operating principle is deliberatively analyzed, the influence of the concave mirror curvature radius on the emerging beam evolution is acquired, the functional relation between the normalized central intensity of the emerging beam, the beam spot size, and NaCl solution concentration is further developed by fit linear method, and the mathematical statistics results reach high precision and linearity. It is expected that the proposed ring resonator sensor and the corresponding conclusions can be useful for precise optical measurement, especially for food safety inspection and medical services of health care.

1. Introduction

The ring resonator [1, 2] is one of the significant appliances in laser optics. It is a kind of traveling wave resonator owning the advantages of low noise, the single frequency wave output, and good frequency characteristic. Meanwhile, this ring resonator can effectively suppress the standing wave effect and the spatial hole burning, which can be widely used in developing high precision laser measurement, precision spectroscopy, frequency measurement, and coherent information processing. Ring resonator structure is an effective method to obtain high power traveling wave laser in a variety of optical precision detection fields; most sensors, such as four frequency differential laser gyros [3] and fiber interferometer filter [4], are composed partially by making use of it. These sensors, which possess the properties of high accuracy, strong ability to resist severe environment, long-lasting life spans, and broad dynamic range [5, 6], are widely applied to measure the physical quantity [7], biochemical quantity [8], biomass parameter [9], and so on.

In recent years, attractive attention has been paid to metamaterials, the so-called negative index materials (NIMs) [10–13]. Double negative material (DNM) [14] with simultaneously permittivity ε and permeability μ is also known as left handed material (LHM), whose unusual electromagnetic (EM) properties were firstly proposed by Velesago [15]. In addition, there are single negative materials (SNMs) among which only one of the EM parameters is negative; these materials include the epsilon negative media (ENGM, $\varepsilon < 0$, $\mu > 0$) and the mu negative media (MNGM, $\varepsilon > 0$, $\mu < 0$) [16, 17]. NIMs have many markedly novel phenomena, for instance, large negative lateral shift [18], beam focusing and phase compensation [19], negative refraction EM energy [20], reverse Doppler Effect [21], inverse Cerenkov radiation [22], etc. These novel characteristics are widely employed in designing periodic-structure like the photonic crystal [23] and optical thin film coating [24]. For instance, Pendry once put forward a sandwich slab system in 2000, and he found that the most remarkable application of DNM in the middle of right handed materials (RHMs) is the concept of perfect

lens, which can achieve subwavelength image beyond the diffraction limit [25]. More recently, Kang *et al.* researched the resonant modes in periodic sandwiched photonic multiple quantum well structures (PSPMQWSs) with SNM; they concluded that the omnidirectional resonance modes can be realized by applying two different photonic crystals which contained SNM, and the resonance modes inside the zero-effective phase gap of the PSPMQWSs are insensitive to the incident angle and the scaling of the barrier photonic crystals [26]. We note that the most commonly used incident beam for studying the interaction between light and sandwich slab system is the plane wave or linearly polarized beam, while the resonator is one of the key components of a laser, and the fundamental of the optical resonator theory is the Gaussian beam (GB). GB and its research products have been widely applied to science and technology, communication, and medicine and other fields with the development of high technology and physical optics [27–29].

In this letter, we mainly study the optical properties of the emerging GB propagating in ring resonator sensor; beam evolution in the sandwich slab system is also deduced as particular case in the coming section. The rest of the paper is organized as follows: firstly, the general propagation formula of the GB propagating through the paraxial optical system is calculated in the space domain by light transfer matrix and generalized Huygens-Fresnel integral equation in Section 2. Then, in Section 3, the GB intensity profiles on emergent intersecting surface of slab system and side view of this beam transmitting in each RHM and DNM unit are explored; the emerging beam spot size changed with negative refractive index coefficient is acquired as well. Furthermore, a ring resonator sensor which can detect the concentration of NaCl solution is designed for what is convinced of to be the first time. Finally, some important conclusions are summarized in Section 4.

2. Physical Model and Formula

The schematic drawing of periodic sandwich slab system is depicted in Figure 1; it is made of two different kinds of textures, the medium layer with red colour stands for RHM, and the light green material stuck between two RHMs is NIM; here we choose isotropic DNM with its relative permittivity and permeability given by the Drude model [30]

$$\varepsilon_r(\omega) = 1 - \frac{\omega_{pe}^2}{\omega^2}, \tag{1}$$

$$\mu_r(\omega) = 1 - \frac{\omega_{pm}^2}{\omega^2}, \tag{2}$$

where ω_{pe} and ω_{pm} are the electric plasma frequency and the magnetic plasma frequency, respectively, the frequency $\nu=\omega/(2\pi)$ is measured in 10^2 THz, with ω being the angular frequency of the input wave, and the length of each DNM unit is L. In general, the formula for the refractive index of DNM is described as follows:

$$n_l = -\sqrt{\varepsilon_r(\omega)\cdot\mu_r(\omega)}. \tag{3}$$

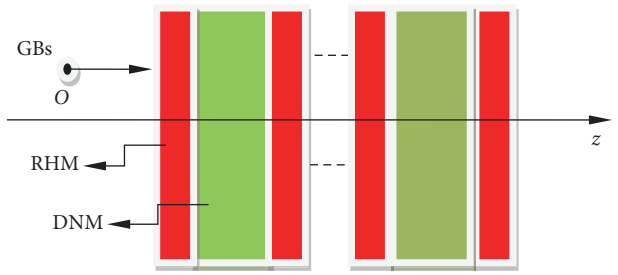

Figure 1: Light path schematic drawing of the sandwich slab system which contained DNM.

With regard to RHM, the refractive index and the length of each unit are n_r and R, respectively.

Considering a cluster of GBs that transmit from point O along the direction of arrow, the electric field at original location (point O) can be described [31]

$$E_1(x_0, y_0, z=0) = \exp\left(-\frac{{x_0}^2 + {y_0}^2}{\omega_0^2}\right), \tag{4}$$

where ω_0 is beam waist radius; x_0 and y_0 are horizontal size and vertical size in the initial location. The normalized beam intensity distribution in any paraxial intersecting surface of the slab system can be described by the generalized Huygens-Fresnel integral equation [32, 33]

$$E_2(x, y, z) = \left(\frac{-i}{\lambda B}\right) e^{ikz} \iint_{s_1} E_1(x_0, y_0, 0) \cdot e^{((ik/2B)[A(x_0^2+y_0^2)+D(x^2+y^2)-2(xx_0+yy_0)])} dx_0\, dy_0, \tag{5}$$

where λ=632.8nm is the wave length of the GB and $k=2\pi/\lambda$ is the wave number. A, B, C, and D are the elements of the total transfer matrix T [34, 35]

$$T = \begin{pmatrix} A & B \\ C & D \end{pmatrix}. \tag{6}$$

While each linear optical element also has its transmission matrix, e.g.,

$$L(x) = \begin{pmatrix} 1 & x \\ 0 & 1 \end{pmatrix} \tag{7}$$

expresses the transfer matrix of wave traveling x distance in the free space,

$$Q(n_r, n_l) = \begin{pmatrix} 1 & 0 \\ 0 & \frac{n_r}{n_l} \end{pmatrix} \tag{8}$$

denotes transfer matrix of RHM-DNM interface when beam propagates from RHM into DNM slab. Similarly, DNM-RHM interface transfer matrix is

$$Q\left(n_l, n_r\right) = \begin{pmatrix} 1 & 0 \\ 0 & \dfrac{n_l}{n_r} \end{pmatrix}. \tag{9}$$

$$R\left(f\right) = \begin{pmatrix} 1 & 0 \\ -\dfrac{1}{f} & 1 \end{pmatrix} \tag{10}$$

denotes transfer matrix of wave reflecting in a concave mirror, where f=r/2 indicates its focal length and r is curvature radius of the concave mirror.

By cross-producing these matrices in accordance with the order of the wave transmission, we obtain the electric field distribution equation of GB propagating through the paraxial slab system in space domain

$$E_2\left(x, y, z\right) = \frac{(ik/2B)\exp\left[-(ikD/2B)\left(x^2 + y^2\right)\right]}{1/\omega_0^2 + ikA/2B} \cdot \exp\left[-\frac{(kx/B)^2 + (ky/B)^2}{4\left(1/\omega_0^2 + ikA/2B\right)}\right]. \tag{11}$$

The beam spot radius can be deduced as the following form:

$$\omega_z = \omega_0\sqrt{A^2 + \left[\frac{B\lambda}{\pi\omega_0^2}\right]^2}, \tag{12}$$

and the beam intensity is easily received by using complex conjugate of $E_2(x, y, z)$

$$I = \frac{n_0}{2c\mu_0}\left|E_2\left(x, y, z\right)\right|^2 \propto \left|E_2\left(x, y, z\right)\right|^2, \tag{13}$$

where c and μ_0 are the speed of light and permeability in vacuum and n_0 denotes the refractive index of wave propagating in free space.

3. Results and Discussion

Firstly, we exhibit transverse normalized intensity distribution of GB before and after wave passing through the whole slab system $(\mathrm{ABA})_m$ with three negative refractive indexes, where A and B stand for RHM and DNM, respectively, m=1 is for the sake of simulation. Here, we choose lossless DNM and its related parameters are set as ω_{pe}=ω_{pm}=$2\pi\nu \times \sqrt{2}$, $2\pi\nu \times \sqrt{2.55}$, and $2\pi\nu \times \sqrt{3.1}$, where ν=c/λ=4.74×10^{14}Hz, leading to corresponding refractive indexes n_l=-1.00, -1.55, and -2.10, respectively. n_r=1.55 fixed, ω_0=0.1mm, the Rayleigh length of this beam is Z_R=$\pi{\omega_0}^2/\lambda$=4.9646cm, and R=2.5Z_R and L=5.0Z_R remain unchanged. It is easily recognized from Figures 2(a2) and 2(b1) that the incident GB and emerging GB outline look exactly alike while DNM n_l= -n_r=-1.55. When n_l=-2.1, the emerging beam maximum intensity slightly decreases along with the increased spot size seen from colour bar of Figure 2(b2). With regard to n_l=-1.0 in Figure 2(b3), not merely the emerging beam maximum intensity decays to 0.24 of the incident beam, but also the spot size increases considerably on output intersecting surface; thus, the output beam quality is relatively poor. The emerging beam spot radius changed with negative refractive index coefficient is also displayed in Figure 2(c).

In order to show how wave transmits from RHM to DNM, we further display the side intensity view of GB propagating in $(\mathrm{ABA})_1$ with three negative refractive indexes in Figure 3; pale yellow arrow lines show the material boundaries. It is easily discovered from Figure 3(a1) that the spot size enlarges while wave propagates in RHM; when it passes through the RHM-DNM interface, the GB undergoes negative refraction; put another way, both incident beam and refracted beam are on the same side of the interface normal; then, beam radius gradually shrinks to its original feature and increases again in the rest of the first DNM. When n_l= -n_r=-1.55, R=2.5Z_R, and R: L: R=1:2:1, enlarged spot size could be compensated exactly while GB transmits in the adjacent material; hence, the intensity profiles of incident beam and emerging beam are completely the same, the corresponding beam evolution principle diagram is depicted in Figure 3(a2). As to n_l=-2.1, R=2.5Z_R, and L =5.0Z_R, the location of the incident beam profile reappeared in DNM is longer than 2.5Z_R; therefore, the emerging beam diverges slightly at the end of second RHM in Figure 3(b1). Now, we need to illustrate the accurate location while beam goes back to its original profile in the middle DNM; when GB passes through the first RHM and DNM, the transfer matrix T can be indicated as

$$\begin{aligned} T &= \begin{pmatrix} A & B \\ C & D \end{pmatrix} \\ &= \begin{pmatrix} 1 & 0 \\ 0 & n_l \end{pmatrix} \times \begin{pmatrix} 1 & L \\ 0 & 1 \end{pmatrix} \times \begin{pmatrix} 1 & 0 \\ 0 & \dfrac{n_r}{n_l} \end{pmatrix} \times \begin{pmatrix} 1 & R \\ 0 & 1 \end{pmatrix} \\ &\quad \times \begin{pmatrix} 1 & 0 \\ 0 & \dfrac{1}{n_r} \end{pmatrix}, \end{aligned} \tag{14}$$

Substituting R=2.5Z_R, n_r=1.55, and n_l=-2.10 into (14), the analytical transmission matrix element B can be expressed as

$$B = -\frac{10}{21} \times L + \frac{625 \cdot \pi}{24521}, \tag{15}$$

and thus, the accurate location to compensate beam divergence in RHM is 3.5Z_R, and the length of total DNM is L=2×3.5Z_R=7.0Z_R; we depict the sandwich slab system with R= 2.5Z_R and L=7.0Z_R arranged in Figure 3(b2); it is clearly seen that the emerging beam intensity gets back to its original feature at the end of RHM. Inversely, the accurate location for n_l=-1.0, R=2.5Z_R is shorter than 2.5Z_R while beam goes back to its original profile in DNM, and the spot size more than double increases at the end of DNM if L=5.0Z_R fixed; therefore, the emerging beam could not come back to its original feature, as shown in Figure 3(c1). By substituting

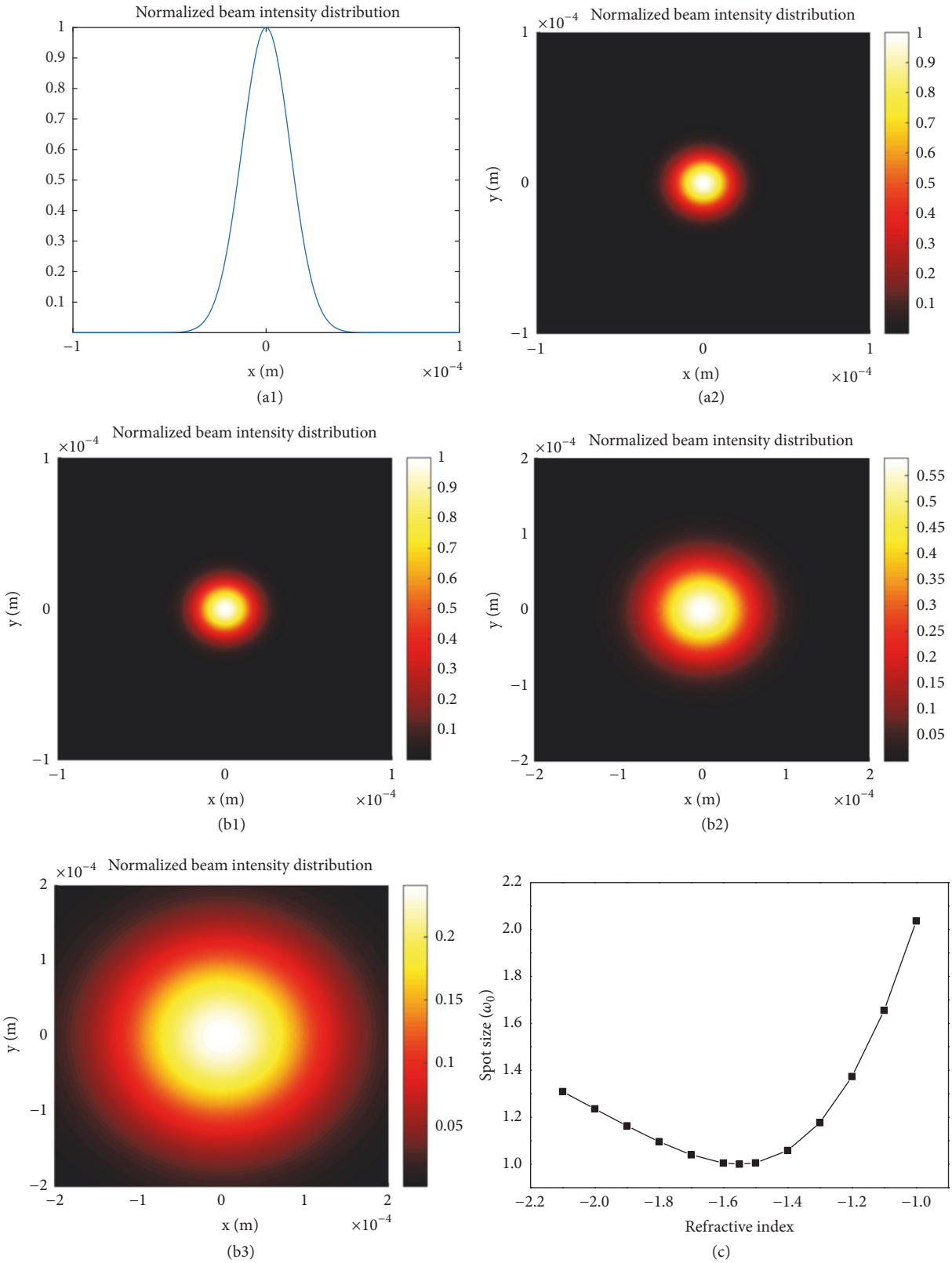

FIGURE 2: Optical parameters of GB versus different negative refractive indexes with m=1, ω_0=0.1×10^{-3}m, n_r=1.55, Z_R =4.9646cm, L=5.0Z_R, R=2.5Z_R, and λ=632.8nm fixed: (a1) incident beam distribution, 1D; (a2) incident beam distribution, 2D; (b1) emerging beam distribution, DNM ω_{pe}=ω_{pm}=2$\pi\nu \times \sqrt{2.55}$; (b2) emerging beam distribution, DNM ω_{pe}=ω_{pm} =2$\pi\nu \times \sqrt{3.1}$ and (b3) emerging beam distribution, DNM ω_{pe}=ω_{pm} =2$\pi\nu \times \sqrt{2}$; (c) beam spot size distribution curve.

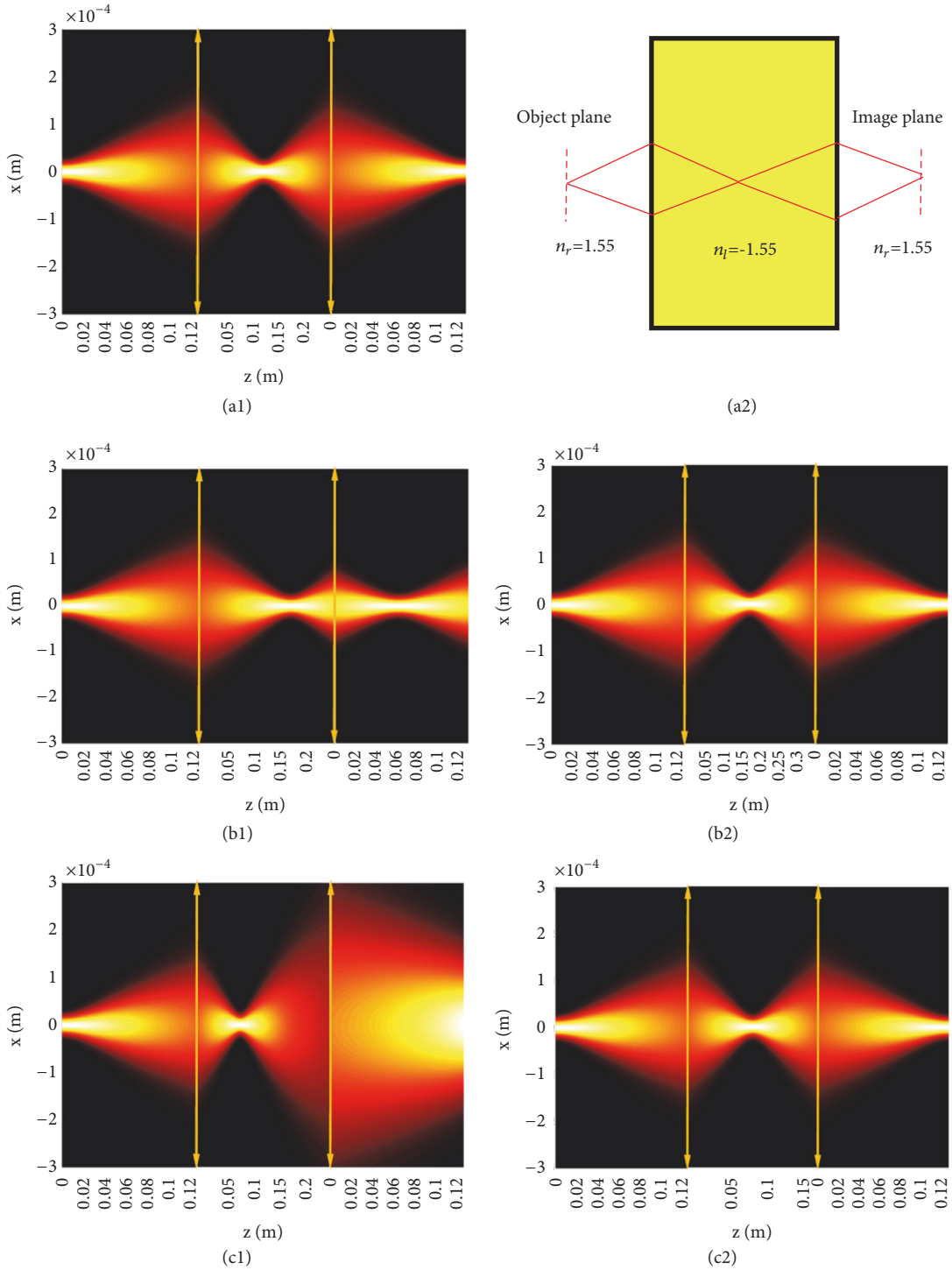

FIGURE 3: Side view of GB propagating in each RHM and DNM unit successively with three kinds of DNMs, $\omega_0=0.1\times10^{-3}$m, $n_r=1.55$, $Z_R=4.9646$cm, and $\lambda=632.8$nm fixed: (a1) DNM $\omega_{pe}=\omega_{pm}=2\pi\nu\times\sqrt{2.55}$; (a2) principle diagram of the emerging GB comes back to its original feature; (b1) DNM $\omega_{pe}=\omega_{pm}=2\pi\nu\times\sqrt{3.1}$; (b2) beam transmission in sandwich slab system, $R=2.5Z_R$, $L=7.0Z_R$, (c1) DNM $\omega_{pe}=\omega_{pm}=2\pi\nu\times\sqrt{2}$ and (c2) beam transmission in sandwich slab system, $R=2.5Z_R$, $L=3.4Z_R$.

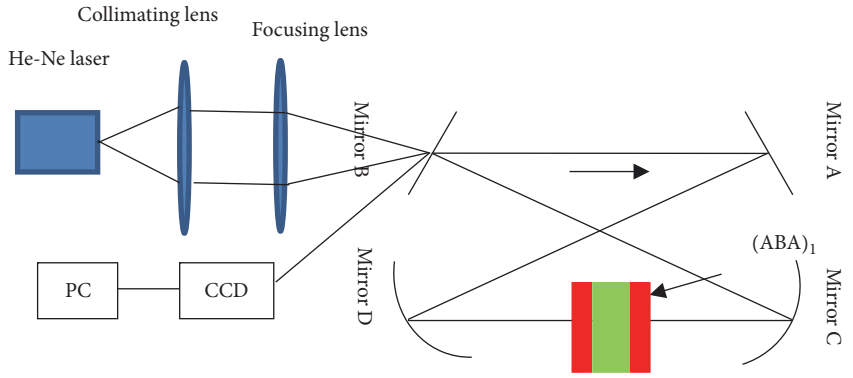

Figure 4: Light path schematic diagram of ring resonator sensor.

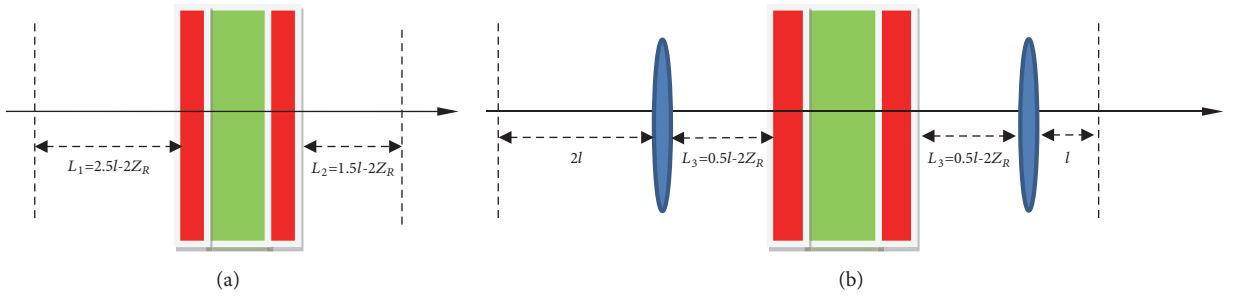

Figure 5: Equivalent lens sequence diagram of ring resonators for two kinds of curvature radius, ω_0=0.1×10^{-3}m, n_r=1.55, $\omega_{pe}=\omega_{pm}=2\pi\nu\times\sqrt{2.55}$, Z_R=4.9646cm, $L=2Z_R$, $R=Z_R$, l=0.2m, and λ=632.8nm fixed: (a) $r\longrightarrow\infty$; (b) r=0.2m.

R= 2.5Z_R, n_r=1.55, and n_l=-1.00 into (14), analytical transfer matrix element B can be also written as

$$B=-L+\frac{625\cdot\pi}{24521}, \tag{16}$$

and thus, the length of the middle DNM is L=2×1.7Z_R=3.4Z_R. The side intensity view of GB propagating in this structural model with R= 2.5Z_R and L=3.4Z_R is demonstrated in Figure 3(c2); the simulation result agrees well with our theoretical analysis.

In this subsection, we propose a ring resonator sensor to measure the concentration of NaCl based on the above theories. In general, there are two independent-positive and negative-traveling wave modes in a bidirectional ring resonator; unidirectional ring resonators are also widely available and have higher output power [36]. Rotatory components which form and split the left and right circular polarization modes in ring cavity [37] ensure the stable output signal of laser with lower loss and backscatter. Besides, the prism, including plane mirror and concave mirror, and active medium [38] are also indispensable elements for this ring resonator. Concave mirror can realize beam focusing and cavity stabilization, while the plane mirror is used to change the direction of wave path. We choose the He-Ne laser, collimating lens, and focusing lens to guide the GB into this ring resonator; the schematic diagram of this ring resonator is shown in Figure 4 [39]. Mirror A and Mirror B represent plane mirrors; Mirror C, Mirror D are the concave mirrors with radius of curvature r=0.2m, the single cavity length is l=0.2m, He-Ne laser with its output wavelength λ=632.8nm is installed outside of the whole cavity, the sandwich slab system $(ABA)_1$ is located in the center of the two concave mirrors, here, A is the space resounded with NaCl solution, B stands for DNM with its n_l=-1.55 fixed, L=2Z_R, and R=Z_R so as to match the standard size of ring resonator sensor.

We begin to discuss the influence of the concave mirror curvature radius on the evolution of the emerging beam while GB propagates a circle in the ring resonator along the arrow line marked in Figure 4. The equivalent lens sequence diagram of ring resonator for $r\longrightarrow\infty$ and r=0.2m is depicted in Figure 5. As we know, the concave mirror will convert into the plane mirror in the condition of $r\longrightarrow\infty$, at this time, the transfer matrix in (10) degrades into

$$R(f\longrightarrow\infty)=\begin{pmatrix}1&0\\0&1\end{pmatrix}. \tag{17}$$

Hence, the GB transmission characteristics in the ring resonator are installed with four plane mirrors more like that in the sandwich slab, except for the extra transmission distance in free space, as shown in Figure 5(a). The corresponding beam intensity distribution for $r\longrightarrow\infty$ and r=0.2m is demonstrated in Figure 6 as well. We can come to the conclusion that the smaller the curvature radius is, the

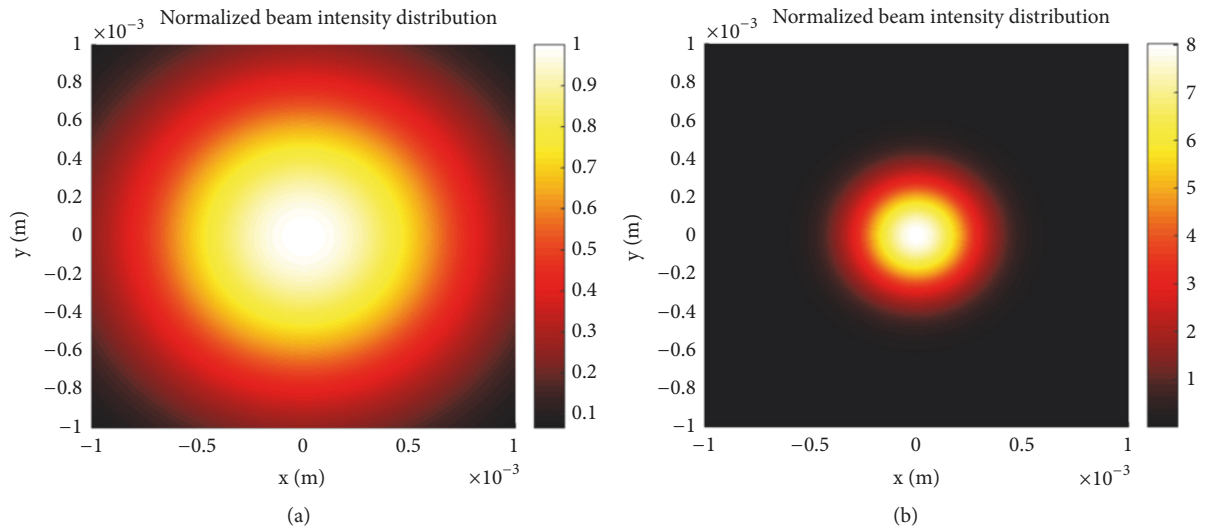

FIGURE 6: Emerging beam intensity distribution when GB propagates a circle in the ring resonator for two kinds of curvature radius, ω_0=0.1×10^{-3}m, n_r=1.55, ω_{pe}=ω_{pm}=2$\pi\nu\times\sqrt{2.55}$, Z_R=4.9646cm, L=2Z_R, R=Z_R, l=0.2m, and λ=632.8nm fixed: (a) $r\longrightarrow\infty$; (b) r=0.2m.

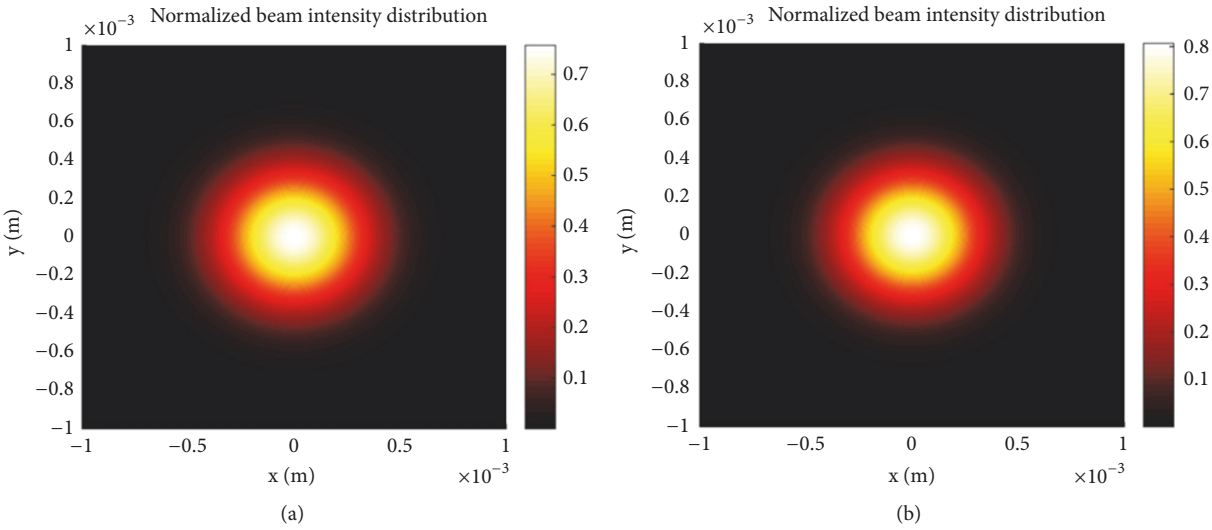

FIGURE 7: Normalized beam intensity distribution of emerging beam on plane Mirror B cross section for different concentration of NaCl solution, ω_0=0.1×10^{-3}m, ω_{pe}=ω_{pm}=2$\pi\nu\times\sqrt{2.55}$, Z_R=4.9646cm, L=2Z_R, R=Z_R, l=0.2m, r=0.2m, and λ=632.8nm fixed: (a) purified water and (b) 25% NaCl solution.

larger the maximum beam intensity is formed, because the focusing ability of a concave mirror is strengthened with the decreasing of curvature radius.

Now, let us discuss how to measure the concentration of NaCl by using the ring resonator sensor. When GB propagates a circle along the allow line marked in Figure 4, the contour profiles for purified water and 25% NaCl solution on output intersecting surface plane of Mirror B are exhibited in Figure 7. Visually, the central bright intensity of 25% NaCl solution is larger than that of purified water discerned from colour bar. With regard to spot size, the quantity value of purified water is a bit bigger, which can be detected by CCD or oscillograph.

In order to have a better understanding of the operating principle of this ring resonator sensor, let us expand the analysis as follows.

The empirical formula between NaCl concentration and its refractive index is [40]

$$N = 1.3331 + 0.00185 \times C, \tag{18}$$

where N is refractive index and C is NaCl concentration. When various kinds of NaCl solution are filled with space A, the relation between normalized maximum intensity, the spot size, and solution refractive index is displayed in Figure 8. It is acquired that the central maximum intensity gradually becomes larger with the increasing of refractive index of NaCl

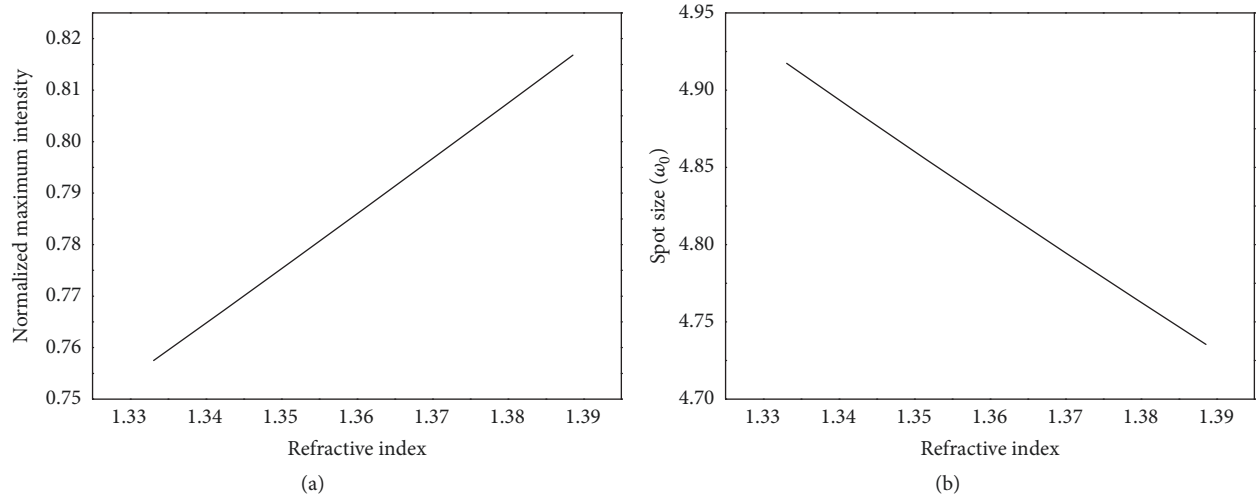

FIGURE 8: Relation between optical parameters of GB and NaCl solution refractive index, ω_0=0.1×10^{-3}m, n_r=1.55, ω_{pe}=ω_{pm}=2$\pi\nu$ × $\sqrt{2.55}$, Z_R=4.9646cm, L=2Z_R, R=Z_R, l=0.2m, r=0.2m, and λ=632.8nm fixed: (a) beam intensity distribution curve; (b) beam spot size curve.

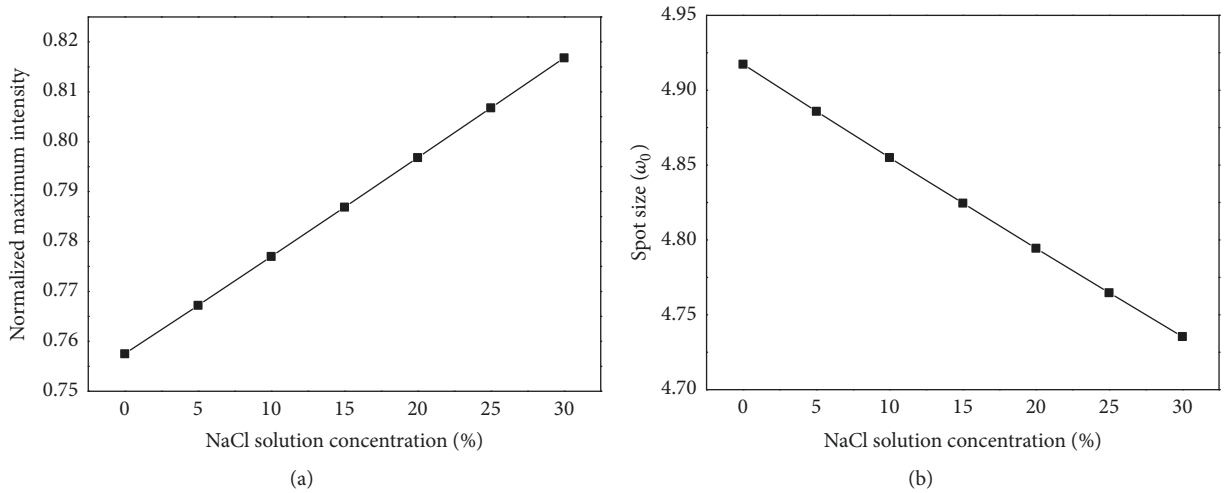

FIGURE 9: Relation between optical parameters of GB and NaCl solution concentration, ω_0=0.1×10^{-3}m, n_r=1.55, ω_{pe}=ω_{pm}=2$\pi\nu$ × $\sqrt{2.55}$, Z_R=4.9646cm, L=2Z_R, R=Z_R, l=0.2m, r=0.2m, and λ=632.8nm fixed: (a) beam intensity distribution curve; (b) beam spot size curve.

solution; by contrast, the larger the refractive index of NaCl solution is, the smaller the spot size is formed, indicating that the NaCl concentration can affect the evolution of the GB as well as other RHM. What is more, both the curves in Figure 8 possess good linear features, which provides reliable guarantee for next precise measurements. In the next moment, the normalized central GB intensity and beam spot size on plane Mirror B cross section changed with a series of NaCl concentration are illustrated as well. The ultimateness is exhibited in Figure 9 and reaches high linearity in coincidence with our assumption. We make use of fit linear method to exhibit the function equation between normalized maximum intensity of emerging GB intensity, its spot size value, and NaCl solution concentration; the quantitative function formulae are

$$I = 0.00198 \times C + 0.75733, \tag{19}$$

where I signifies normalized central intensity. The statistics of Adjusted R-square and Residual Sum of Squares of this formula reach 0.99997 and 7.67857×10^{-8}. And

$$\omega_z = 4.91625 - 0.00606C, \tag{20}$$

and the statistics parameters of above formula are 0.99983 and 3.56536×10^{-6}, respectively. Just as we described above, this ring resonator sensor demonstrates excellent linear correlation and statistics; we are certain that the rational using of it in concentration detection will become a necessary and useful supplement to the chemical sensor.

To the best of our knowledge, this ring resonator sensor can probe other solutions like sucrose, Na_2CO_3, and so on in so far as the parameters of intercept and slope of (19) and (20) are adjusted. It is expected that the proposed ring resonator sensor and the corresponding conclusions can be

useful for precise optical measurement, especially for food safety inspection and medical services of health care.

4. Summary

In conclusion, we have researched the evolution of GB propagating in the sandwich slab system based on the light transfer matrix and generalized Huygens-Fresnel integral equation. It is revealed that the emerging GB can come back to its original feature by using the sandwich slab system which contained negative index material as long as the negative refractive index n_l=- n_r and each unit length R:Z:R=1:2:1; while $n_l \neq$ - n_r, the larger abs(n_l) is, the longer DNM is needed to achieve emerging beam reconstruction and vice versa. The emerging beam spot size changed with negative refractive index coefficient is also acquired. Meanwhile, we propose a ring resonator sensor to measure the concentration of NaCl, whose operating principle, especially the influence of the concave mirror curvature radius on the emerging beam evolution, is deliberatively analyzed. The functional relation between normalized central intensity, beam spot size, and NaCl solution concentration is given by (19) and (20), respectively, and assuredly reaches high precision and linearity. It is expected that the proposed ring resonator sensor and the corresponding conclusions can be useful for precise optical measurement, especially for food safety inspection and medical services of health care.

Data Availability

The data used to support the findings of this study are available from the corresponding author upon request.

Conflicts of Interest

The authors declare that there are no conflicts of interest regarding the publication of this paper.

Acknowledgments

This work was supported by the financial support from the College Innovation Training Program of Hubei University of Automotive Technology in China (nos. DC 2018090 and DC2018099).

References

[1] S. I. Bozhevolnyi, V. S. Volkov, E. Devaux, J. Y. Laluet, and T. W. Ebbesen, "Channel plasmon subwavelength waveguide components including interferometers and ring resonators," *Nature*, vol. 440, no. 7083, pp. 508–511, 2006.

[2] H. Qiu, T. Kurihara, H. Harada et al., "Enhancing terahertz magnetic near field induced by a micro-split-ring resonator with a tapered waveguide," *Optics Expresss*, vol. 43, no. 8, pp. 1658–1661, 2018.

[3] J. Yuan, M. Chen, Y. Li, Z. Tan, and Z. Wang, "Reanalysis of generalized sensitivity factors for optical-axis perturbation in nonplanar ring resonators," *Optics Express*, vol. 21, no. 2, pp. 2297–2306, 2013.

[4] J. Xu, L. Huang, S. Yin, B. Gao, and P. Chen, "All-fiber self-mixing interferometer for displacement measurement based on the quadrature demodulation technique," *Optical Review*, vol. 25, no. 1, pp. 40–45, 2018.

[5] G. Sanders, "Fiber optic gyros for space, marine, and aviation applications," *Proceedings of SPIE -The International Society for Optical Engineering*, vol. 283712, no. 12, pp. 61–71, 1996.

[6] Z. Wang, X. Long, and F. Wang, "Overview of four-mode differential laser gyros," *Laser & Optoelectronics Progress*, vol. 49, no. 4, article 040005, 2012.

[7] Q. Xu, S. Sandhu, M. L. Povinelli, J. Shakya, S. Fan, and M. Lipson, "Experimental realization of an on-chip all-optical analogue to electromagnetically induced transparency," *Physical Review Letters*, vol. 96, no. 12, article 123901, 2006.

[8] C. Ciminelli, C. M. Campanella, F. Dell'Olio, C. E. Campanella, and M. N. Armenise, "Label-free optical resonant sensors for biochemical applications," *Progress in Quantum Electronics*, vol. 37, no. 2, pp. 51–107, 2013.

[9] M. Bahadoran, A. F. A. Noorden, K. Chaudhary et al., "Modeling and analysis of a microresonating biosensor for detection of salmonella bacteria in human blood," *Sensors*, vol. 14, no. 7, pp. 12885–12899, 2014.

[10] J. Valentine, S. Zhang, T. Zentgraf et al., "Three-dimensional optical metamaterial with a negative refractive index," *Nature*, vol. 455, no. 7211, pp. 376–379, 2008.

[11] H. J. Lezec, J. A. Dionne, and H. A. Atwater, "Negative refraction at visible frequencies," *Science*, vol. 316, no. 5823, pp. 430–432, 2007.

[12] M. Sadatgol, Ş. K. Özdemir, L. Yang et al., "Plasmon injection to compensate and control losses in negative index metamaterials," *Physical Review Letters*, vol. 115, no. 3, article 035502, 2015.

[13] S. Lan, L. Kang, D. T. Schoen et al., "Backward phase-matching for nonlinear optical generation in negative-index materials," *Nature Materials*, vol. 14, no. 8, pp. 807–811, 2015.

[14] M. J. Hossain, M. R. I. Faruque, and M. T. Islam, "Design and analysis of a new composite double negative metamaterial for multi-band communication," *Current Applied Physics*, vol. 17, no. 7, pp. 931–939, 2017.

[15] V. G. Veselago, "The electrodynamics of substances with simultaneously negative values of ε and μ," *Soviet Physics Uspekhi*, vol. 10, no. 4, pp. 509–514, 1968.

[16] H. N. Hajesmaeili, M. Zamani, and M. H. Zandi, "Bi-gyrotropic single-negative magnetic materials in the presence of longitudinal magnetization: a transfer matrix approach," *Photonics and Nanostructures: Fundamentals and Applications*, vol. 24, no. 5, pp. 69–75, 2017.

[17] W. Liu, Y. Yuan, T. Tang et al., "Band gap characteristics of photonic crystals consisted of left-handed material in the microwave band," *Acta Photonica Sinica*, vol. 45, no. 2, article 216002, Article ID 216002, 2016.

[18] Y.-Q. Kang, W. Ren, and Q. Cao, "Large tunable negative lateral shift from graphene-based hyperbolic metamaterials backed by a dielectric," *Superlattices and Microstructures*, vol. 120, no. 8, pp. 1–6, 2018.

[19] Q. Li, L. Huang, H. So, H. Xue, and P. Zhang, "Beam pattern synthesis for frequency diverse array via reweighted *l*_1 iterative phase compensation," *IEEE Transactions on Aerospace & Electronics Systems*, vol. 54, no. 1, pp. 467–475, 2018.

[20] D. Dahal and G. Gumbs, "Effect of energy band gap in graphene on negative refraction through the veselago lens and electron conductance," *Journal of Physics and Chemistry of Solids*, vol. 100, no. 1, pp. 83–91, 2017.

[21] A. V. Chumak, P. Dhagat, A. Jander, A. A. Serga, and B. Hillebrands, "Reverse doppler effect of magnons with negative group velocity scattered from a moving bragg grating," *Physical Review B - Condensed Matter and Materials Physics*, vol. 81, no. 14, article 140404, 2010.

[22] B. Wu, J. Lu, J. Kong, M. Chen, and Z. Duan, "Cherenkov radiation in anisotropic double-negative metamaterials," *Optics Express*, vol. 16, no. 22, pp. 18479–18484, 2008.

[23] S. A. El-Naggar, "Photonic gaps in one dimensional cylindrical photonic crystal that incorporates single negative materials," *The European Physical Journal D*, vol. 71, no. 1, pp. 11–16, 2017.

[24] Y.-J. Jen, C.-H. Chen, and C.-W. Yu, "Deposited metamaterial thin film with negative refractive index and permeability in the visible regime," *Optics Expresss*, vol. 36, no. 6, pp. 1014–1016, 2011.

[25] J. B. Pendry, "Negative refraction makes a perfect lens," *Physical Review Letters*, vol. 85, no. 18, pp. 3966–3969, 2000.

[26] Y. Kang and C. Zhang, "Resonant modes in photonic multiple quantum well structures with single-negative materials," *Optik - International Journal for Light and Electron Optics*, vol. 124, no. 22, pp. 5430–5433, 2013.

[27] M. C. Gökçe and Y. Baykal, "Aperture averaging and BER for Gaussian beam in underwater oceanic turbulence," *Optics Communications*, vol. 410, pp. 830–835, 2018.

[28] K.-S. Cheng and R. B. Roemer, "Blood perfusion and thermal conduction effects in Gaussian beam, minimum time single-pulse thermal therapies," *Medical Physics*, vol. 32, no. 2, pp. 311–317, 2005.

[29] Z. Xiang, Y. Yuan, C. Li et al., "Multiple reflections and fresnel absorption of gaussian laser beam in an actual 3d keyhole during deep-penetration laser welding," *International Journal of Optics*, vol. 2012, Article ID 361818, 8 pages, 2012.

[30] S. A. Cummer, "Dynamics of causal beam refraction in negative refractive index materials," *Applied Physics Letters*, vol. 82, no. 13, pp. 2008–2010, 2003.

[31] Y. Gao, Z. An, N. Li, W. Zhao, and J. Wang, "Optical design of Gaussian beam shaping," *Optics & Precision Engineering*, vol. 19, no. 7, pp. 1464–1471, 2011.

[32] B. Lü, *Laser Optics-Beam Characterization, Propagation and Transformation, Resonator Technology and Physics*, Higher Education Press, Beijing, China, 3rd edition, 2003.

[33] L. Jin and X. Zhang, "Propagation properties of airy beam through periodic slab system with negative index materials," *International Journal of Optics*, vol. 2018, Article ID 9478483, 7 pages, 2018.

[34] S. Wang and L. Ronchi, "II principles and design of optical arrays," *Progress in Optics*, vol. 25, no. 1, pp. 279–348, 1988.

[35] J. Zhou, H. Luo, S. Wen, and Y. Zeng, "ABCD matrix formalism for propagation of Gaussian beam through left-handed material slab system," *Optics Communications*, vol. 282, no. 14, pp. 2670–2675, 2009.

[36] C. Du, G. Liao, L. Zhang et al., "Design and experimental research of laser with four-mirror ring resonator," *Laser & Infrared*, vol. 42, no. 1, pp. 26–30, 2012.

[37] S. Berg, T. Prellberg, and D. Johannsmann, "Nonlinear contact mechanics based on ring-down experiments with quartz crystal resonators," *Review of Scientific Instruments*, vol. 74, no. 1, pp. 118–126, 2003.

[38] Y. Honda, H. Shimizu, M. Fukuda et al., "Stabilization of a non-planar optical cavity using its polarization property," *Optics Communications*, vol. 282, no. 15, pp. 3108–3112, 2009.

[39] L. Jin and X. Zhang, "Wave transmission characteristics in ring cavity containing meta-materials," *Semiconductor Optoelectronics*, vol. 38, no. 1, pp. 66–69, 2017.

[40] Z. Bai, Z. Liu, and H. Xu, "An experienced formula about the connection of refraction index and consistence of several liquid," *Journal of Yanan University (Natural Science Edition)*, vol. 23, no. 1, pp. 33–36, 2004.